



RESEARCH ARTICLE

10.1029/2017GC007391

Key Points:

- A global scale block model is used to estimate slip-deficit rates across Earth's most active faults
- The 307 blocks and $1.59 \times 10^7 \text{ km}^2$ of fault area explain $>19,600$ GPS velocities to a resolution of 2.2 mm/year
- Seismic moment accumulation rates are compared with historical moment release

Supporting Information:

- Supporting Information S1

Correspondence to:

S. E. Graham,
shannonegraham@fas.harvard.edu

Citation:

Graham, S. E., Loveless, J. P., & Meade, B. J. (2018). Global plate motions and earthquake cycle effects. *Geochemistry, Geophysics, Geosystems*, 19, 2032–2048.
<https://doi.org/10.1029/2017GC007391>

Received 8 DEC 2017

Accepted 15 MAY 2018

Accepted article online 14 JUN 2018

Published online 10 JUL 2018

Global Plate Motions and Earthquake Cycle Effects

Shannon E. Graham^{1,2} , John P. Loveless³ , and Brendan J. Meade¹

¹Department of Earth and Planetary Sciences, Harvard University, Cambridge, MA, USA, ²Now at Boston College, Chestnut Hill, MA, USA, ³Department of Geosciences, Smith College, Northampton, MA, USA

Abstract The rotations of tectonic plates provide a partial description of the total observed displacements at the Earth's surface. The estimated number of kinematically distinct plates has increased from 12 in 1990 to 56 in 2010 as a result of the increase in the number of kinematic observables. At length scales $<1,000$ km, rotation-only plate models are inaccurate because geodetic signals of long-term plate motions are complicated by earthquake cycle effects. Here we present results from a global block model that unifies large-scale plate motions and local earthquake cycle effects at plate boundaries. Incorporating the rotations of 307 distinct plates, elastic strain accumulation from 16 subduction zones and $1.59 \times 10^7 \text{ km}^2$ of fault system area, this model explains 19,664 interseismic GPS velocities at a resolution of 2.2 mm/year. Geodetically constrained fault slip deficit rates yield a cumulative global moment accumulation rate of $1.09 \times 10^{22} \text{ N}\cdot\text{m}/\text{year}$, 12% larger than the average annual coseismic moment release rate from 1900 to 2013. The potential contribution to the total moment rate budget can be estimated from the frequency distribution of the modeled fault slip-deficit rates, which follow an exponential distribution. Integrating this frequency distribution over all possible slip rates indicates that the geologic structures included in this reference global block model account for 98% of the global moment budget. Comparing our results with population distribution, we find that $\sim 50\%$ of the world's population lives within 200 km of an active fault with a slip rate >2 mm/year.

1. Introduction

Early global plate motion models (Chase, 1978; Le Pichon, 1968; Minster & Jordan, 1978; Morgan, 1968) used observations of seafloor spreading rates, fault azimuths, and earthquake slip vectors to constrain the rotation rate vectors of 5–12 continental scale tectonic plates. In 1990, a new global plate motion model, NUVEL, was developed by analyzing magnetic profiles across mid-ocean ridges, dense aeromagnetic surveys, transform fault surveys, and centroid-moment tensor focal mechanisms to constrain the late-Cenozoic motions of 12 plates (DeMets et al., 1990). Thirteen years later, Bird (2003) described the boundaries and motions of 52 tectonic plates (ranging in area from $8.2 \times 10^3 \text{ km}^2$ to $1.05 \times 10^8 \text{ km}^2$). In 2010, an update to NUVEL, MORVEL, was introduced, providing a set of rotation rate vectors and uncertainties for 25 tectonic plates accounting for 97.2% of the Earth's surface (DeMets et al., 2010). The NNR-MORVEL56 model (Argus et al., 2011), which provides a set of rotation rate vectors for 56 plates in a no-net-rotation reference frame, includes the 25 plates from MORVEL and 31 additional plates adapted from Bird (2003). While these kinematic plate models adequately describe motion in the center of tectonic plates, they fall short of providing an accurate description of observed deformation at the plate boundaries where earthquake cycle effects are significant.

The Global Strain Rate Model (e.g., GSRMv2.1, Kreemer et al., 2014) demonstrates one method for integrating both large-scale plate motions and deformation at plate boundaries. In GSRMv2.1, $\sim 14\%$ of the Earth's surface is allowed to deform within 145,086 grid cells (sized 0.2° latitude by 0.25° longitude), while the remainder of Earth's surface is treated as rigid bodies that represent tectonic plates. The result is a global model of plate motions and strain rates in plate boundary zones constrained by $\sim 22,500$ horizontal geodetic velocities. Additionally, the seismic hazard inferred from tectonics (SHIFT) equations and assumptions of Bird and Liu (2007) have been applied to strain rates predicted by GSRMv2.1 in order to forecast the seismicity within each of the deforming cells (SHIFT-GSRM2f, Bird & Kreemer, 2015). While the GSRM and SHIFT-GSRM2f models consider deformation and potential seismicity at plate boundaries, these are not localized on any specific fault structure. Herein we describe a global block model (GBM) that unifies global plate motions

©2018. The Authors.

This is an open access article under the terms of the Creative Commons Attribution-NonCommercial-NoDerivs License, which permits use and distribution in any medium, provided the original work is properly cited, the use is non-commercial and no modifications or adaptations are made.

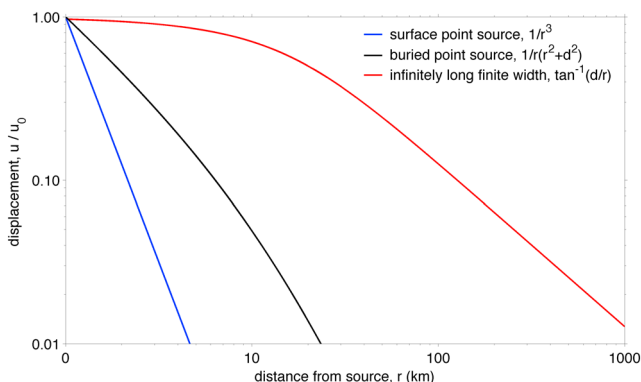


Figure 1. Displacements at a half-space surface as a function of distance, r , from a dislocation source for three cases: a surface point source (blue line), a buried point source (black line), and an infinitely long fault of finite width, d (red line). With an infinitely long fault, displacements fall off at a more gradual rate than $1/r$, and are much slower than for a point source.

Bilham et al., 1997; Feigl et al., 1993; Jouanne et al., 2004; Savage & Burford, 1973), where Earth's surface is assumed to move in a manner that reflects elastic or viscoelastic strain accumulation in the crust or time-dependent deformation in the lower crust/upper mantle. This class of models has been used to constrain fault geometries and the distribution of fault coupling, in addition to serving as a basis for comparison against geologic slip rates (e.g., Segall, 2002). Block modeling extends these models to integrate both earthquake cycle deformation and plate rotations. Regional scale block models have commonly been used to determine fault slip rates and seismic hazard over areas of $\sim 10,000 \text{ km}^2$ (e.g., Japan, Loveless & Meade, 2010; Southern California, McCaffrey et al., 2007; and New Zealand, Wallace et al., 2004).

Linear spherical block theory (Meade & Loveless, 2009) states that interseismic velocities (\mathbf{v}_i) can be decomposed and modeled as a combination of elastic earthquake cycle deformation arising from slip deficit on block-bounding faults, partial coupling on triangular dislocation elements (TDEs) used to represent geometrically complex fault surfaces, and plate rotations. This expression can be written in terms of block rotation vectors, Ω , as $\mathbf{v}_i = \mathbf{v}_B(\Omega) - [\mathbf{v}_{CSD}(\Omega) + \mathbf{v}_{TDE}(\mathbf{t})]$, where (\mathbf{v}_B) is the velocity due to block rotations, \mathbf{v}_{CSD} is the velocity due to elastic deformation from the slip deficit on fully coupled block-bounding faults, \mathbf{v}_{TDE} is the velocity contribution from elastic deformation associated with variably coupled faults parametrized as TDEs, and \mathbf{t} is the TDE slip rate components. A weighted least-squares inversion is used to simultaneously estimate Ω and \mathbf{t} , minimizing the misfit between observed velocities and model predictions. Fault slip rates are then calculated by projecting rotational block motions onto the block-bounding faults, which ensures kinematic consistency. A homogeneous elastic half-space is assumed to calculate the elastic deformation for each fault segment using spherical geometry with locally optimal coordinate transformations to minimize areal distortion.

In the following, we expand the regional model approach to a global scale, thus unifying global plate motion models with local earthquake cycle deformation. One motivation for this is highlighted by the question: What impact may an adjacent region have on a regional-scale block model? If we consider the surface displacements due to the dislocation of surface point source, displacements fall off with distance, r , from the source as $1/r^3$ (Figure 1). However, in the case of an infinitely long fault of finite width (as in the case of a block), displacements fall off more gradually than $1/r$ (Figure 1). This implies that observed velocities in one area may be influenced by earthquake cycle processes in surrounding regions. Herein, we present the model setup, data sources, and results from a reference GBM. Using spherical block theory, we invert 19,664 GPS velocities to estimate fault slip rates, plate motions, and spatially varying interplate coupling along subduction zones, with a mean residual velocity of 2.2 mm/year. We chose not to include intrablock strain in this version of the global model. Bird (2009) find that up to one third of relative plate motion in California is accommodated as permanent strain, and thus areas with large or systematic misfits may represent locations where internal deformation of a block is required to accurately describe interseismic deformation. Likewise, a larger block with internal strain may be able to replace several smaller blocks. These options will be explored in later iterations of the GBM.

with fault-based mechanical earthquake cycle models, resolving slip deficit rates across the world's most seismogenic faults.

The central concept adopted here is that the number of tectonic blocks should be defined as a quantity dependent on the resolution at which we choose to describe motions at the Earth's surface. In other words, the question we want to answer is, "How many blocks and faults are required to describe GPS velocities at n mm/year resolution?" The high precision of modern geodetic measurements leads to the introduction of relatively small ($r \sim 100 \text{ km}$) blocks at plate boundary zones where earthquake cycle effects are large. This also enables us to analyze the statistical distributions of plate areas (Bird, 2003; Sornette & Pisarenko, 2003) and slip deficit rates (Meade, 2007) to determine how many additional structures may be required to explain observations at greater levels of detail.

2. Block Modeling

Earthquake cycle models have long been used to interpret geodetic observations of interseismic crustal deformation at plate boundaries (e.g.,

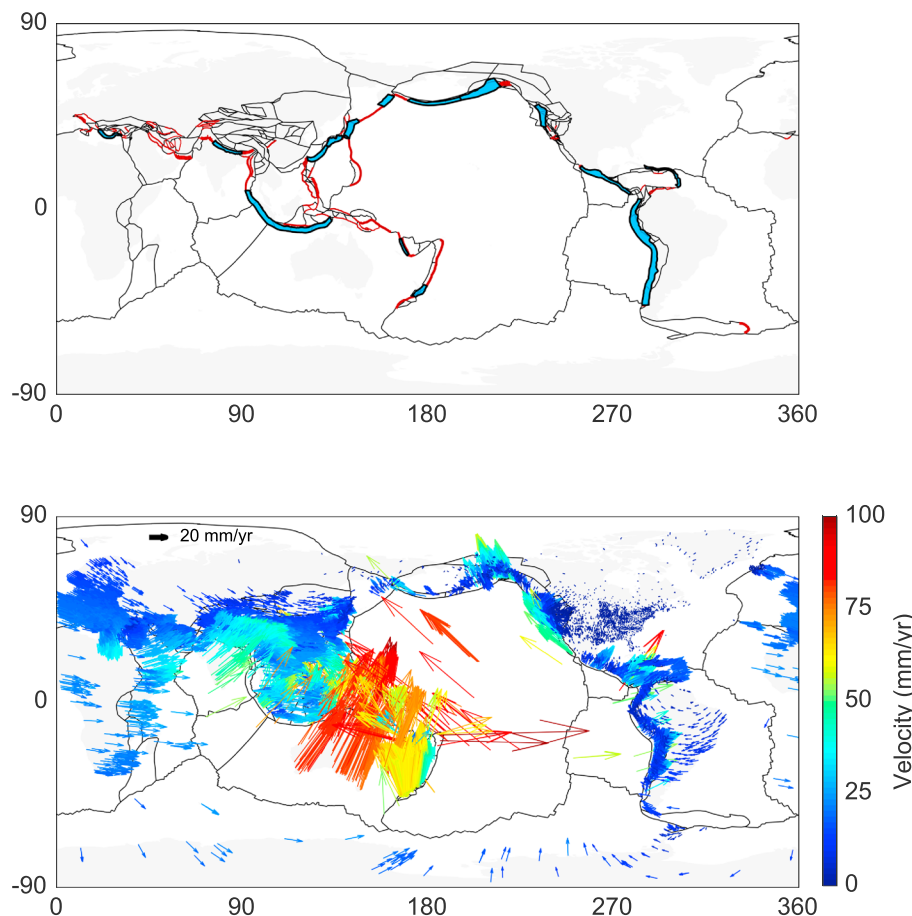


Figure 2. (Top) Block model geometry. Black lines are vertical fault segments. Red segments indicate dipping faults, and blue regions show where networks of triangular dislocation elements are used to define subduction zone interfaces. (Bottom) Global velocity field in NA-fixed reference frame with vectors scaled and colored by velocity.

3. GPS Velocities

To constrain the GBM, we augment the velocity field developed for the Global Strain Rate Model (GSRM v2.1, Kreemer et al., 2014). This velocity field was carefully compiled from >6,000 stations published in online archives and over 15,000 velocities from >230 published studies. The data span January 1996 to December 2013, excluding time series that are shorter than 2.5 years or that contain documented transient motion (e.g., postseismic deformation). We supplement the GSRMv2.1 data with estimated interseismic velocities from Ecuador (Chlieh et al., 2014), western Caribbean (Kobayashi et al., 2014), Peru (Lanza, 2014), Peru and Ecuador (Nocquet et al., 2014), Venezuela (Reinoza et al., 2015), El Salvador (Staller et al., 2016), Panama (Bennett et al., 2014), Mexico (Rousset et al., 2016), New Zealand (Wallace et al., 2012), Papua New Guinea (Wallace et al., 2014), and the Caribbean (COCONet, UNAVCO: <http://www.unavco.org>). Velocities are transformed into a NA-fixed reference frame by solving for rotation and translation vectors which minimize the difference in velocities at collocated stations. Duplicate stations are removed, as well as velocities from Aktug and Kilicoglu (2006) and Aktug et al. (2009) due to unknown contributions to the velocities from coseismic and postseismic sources. The final velocity field for the GBM consists of east and north velocities at 19,664 stations (Figure 2b). This number is less than the total from GSRM after removing duplicate stations from studies that overlapped.

4. Model Construction and Block Geometry

As the starting point for the GBM, we use the tectonic plate geometries from NNR-MORVEL56 (Argus et al., 2011) to define block boundaries. Regional block models from published studies were then incorporated into the NNR-MORVEL56 plate geometry, adding more fault segments and smaller blocks. Where regional block

Table 1
Block Models and Fault Maps From Previous Work Used in Creating the Global Block Model Organized by Region

Region	Study
Aegean	Vernant et al. (2014)
Alaska	Koons et al. (2010); Elliott et al. (2013); Li et al. (2016)
Armenia	Ritz et al. (2016)
Caribbean	Symithe et al. (2015)
Caucasus	Karakhanyan et al. (2013)
Central America/Mexico	Rodriguez et al. (2009); Kobayashi et al. (2014); Bennett et al. (2014) Andria Ellis per. comm. 2015
East Africa Rift	McClusky et al. (2010); Saria et al. (2014)
Iceland	Metzger et al. (2013); Travis (2012)
Indonesia	Baldwin et al. (2012); Koulali et al. (2016)
Iran	Walpersdorf et al. (2014); Reilinger et al. (2006); Djamour et al. (2010); Djamour et al. (2011); Hollingsworth et al. (2008); Mousavi et al. (2013); Peyret et al. (2009); Bayer et al. (2006)
Israel/Jordan/Lebanon/Syria	Le Beon et al. (2008); Reilinger et al. (2006)
Italy	Ventura et al. (2014); Battaglia et al. (2004); DISS Working Group (2010)
Japan	Loveless and Meade (2010)
Myanmar	Socquet et al. (2006); Rangin et al. (2013); Kundu and Gahalaut (2013); Simons et al. (2007)
New Zealand	Wallace et al. (2004); Wallace et al. (2007); Wallace et al. (2012)
Papua New Guinea	Wallace et al. (2014)
Phillippines	Galgana (2009); Socquet et al. (2006); Kreemer et al. (2000); Yu et al. (2013)
South America	Reinoza et al. (2015); Moreno et al. (2011); Métois et al. (2013); Audemard et al. (2000); Machare et al. (2003); Eguez et al. (2003); U.S. Geological Survey and Paris (2000); Veloza et al. (2012)
South Spain/North Africa	Koulali et al. (2011)
Sumatra	Chlieh et al. (2008); DeShon et al. (2005); Mukti et al. (2012); McCaffrey (2009); Michel et al. (2001)
Taiwan	Sun et al. (2015); Shyu et al. (2005); Ching et al. (2011)
Tibet/Asia	Loveless and Meade (2011a); Hubbard et al. (2016); Styron et al. (2010); Taylor and Yin (2009)
Tonga/Vanuatu	Power et al. (2012)
Turkey	Ozener et al. (2010); DeVries et al. (2017); Aktug, Meherremov, et al. (2013); Aktug, Dikmen, et al. (2013); Aktug et al. (2015); Reilinger et al. (2010)
Western US	Evans et al. (2015) Loveless and Meade (2011b); McCaffrey et al. (2013)

models were not available, new blocks were constructed from published fault maps. Table 1 lists all of the studies incorporated into the GBM by region. Blocks containing no stations were removed, as their motions are not well constrained, with two exceptions: The Juan de Fuca and Rivera plates were retained in order to allow for subduction in Cascadia and the northwest portion of the Mexico subduction zone, respectively. The Euler pole locations and rotation rates were fixed for these two blocks as those defined by McCaffrey et al. (2007; Juan de Fuca), and DeMets et al. (2010; Rivera). In total, there are 307 blocks (as compared with the 44 from NNR-MORVEL56 that contain GPS stations from the global velocity field) defined by 446,870 km of fault segments (translating to 1.59×10^7 km² of fault system area). The complete model geometry is shown in Figure 2. However, we note a bias within GBM regarding the distribution and size of the blocks given the nonuniform nature of global geodetic coverage.

We created networks of TDEs to represent 16 of the world's major convergent boundary interfaces, where there is adequate GPS station coverage to estimate spatially variable interseismic coupling (blue regions in Figure 2a). Spatially variable coupling is also allowed on the Parkfield segment of the San Andreas fault.

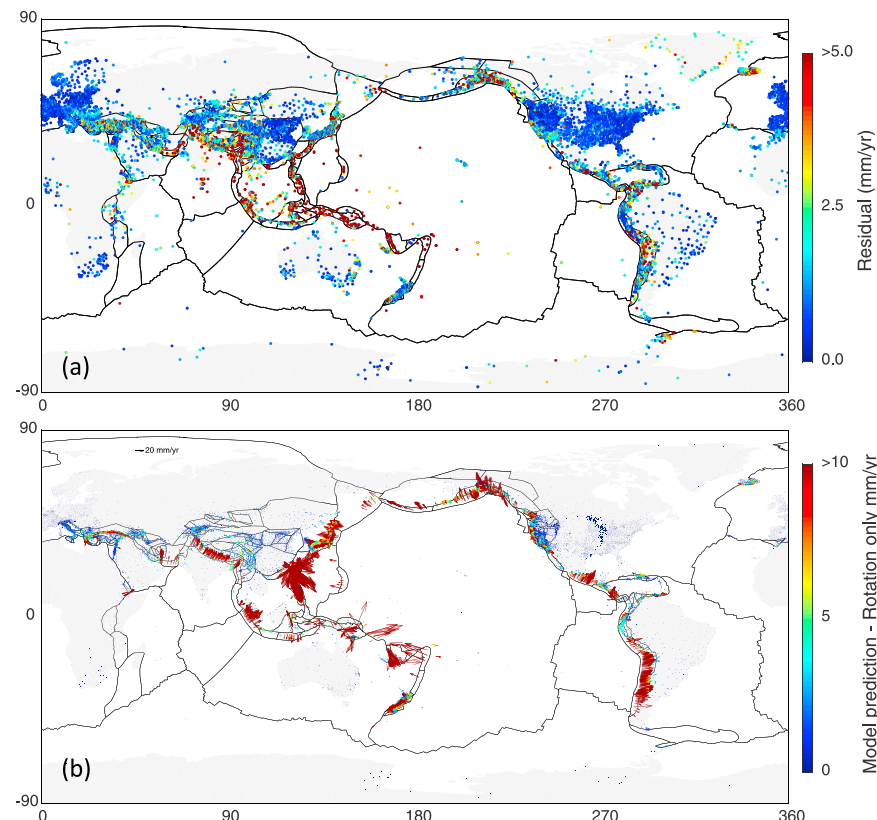


Figure 3. (a) Magnitude of residual velocities (observations minus model predicted) in mm/year for the global block model. The color scale saturates at 5 mm/year. (b) A comparison of velocities predicted by the model and the component of the velocity due solely to block rotation. The color scale saturates at 10 mm/year to highlight regions where block rotations accurately describe observed motion (cool colors), while hot colors emphasize regions that require earthquake cycle processes to explain the data.

Nine of the subduction interface geometries incorporated into the model are based on the Slab1.0 model (Hayes et al., 2012). The remaining seven TDE meshes are based on the following sources: Mexico/Central America—combination of Radiguet et al. (2012) in Mexico and Slab1.0 in Central America; New Zealand—Wallace and Beavan (2010); Japan/Nankai/Sagami—Loveless and Meade (2010); Himalaya—Hubbard et al. (2016); and Caribbean—Symithe et al. (2015). In total, there are 14,140 TDEs incorporated into GBM. For subduction zones without sufficient data to constrain spatially variable coupling, we assume fully coupled rectangular dipping faults set to the average dip of that subduction interface, extended through seismogenic depths for megathrust events (~40 km). Dips and varying locking depths are set on block-bounding faults with known geometries (red segments in Figure 2a). All other fault segments are modeled as vertical with locking depths between 5 and 20 km depending on regional information and set to 15 km, if there are no existing data. Additionally, we apply a priori constraints on 111 fault segments to sparsely regularize the inversion. These include 66 tensile slip, 31 dip-slip, and 14 strike-slip constraints to prevent localized ill-conditioning in regions where GPS data are sparse (see the supporting information). These constraints were determined through trial and error with a focus on minimizing the total number and to ensure that convergence rates at major subduction zones were consistent with previously published estimates. There are no constraints placed on mid-ocean ridge segments either geodetically or geologically/seismologically. All model input files, including fault geometry and any a priori constraints are available through the following Github repository: https://github.com/brendanjmeade/reference_gbm. Results presented herein represent a reference realization of a global scaled block model. We note that there are regions where the model could be modified or adjusted and encourage researchers to add their own improvements into this framework.

5. Results

An inversion of the 39,328 horizontal GPS velocity components with the GBM fault geometry fits the data at a resolution of 2.2 mm/year, within a millimeter of the average uncertainty. The normalized weighted sum-squared residual ($nWSSR$) for the model is 7.04. For comparison, we also invert the same set of observations with 12- and 44-plate models, corresponding to the NUVEL-1a, and NNR-MORVEL56/Bird 2003 plate geometries, with station-less blocks removed and fault locking depths universally set to zero to illustrate the effect of ignoring earthquake cycle processes. These two models feature large residual velocities at plate boundaries (mean residual magnitudes of 10.0 and 7.4 mm/year, respectively; in contrast to GBM (2.2 mm/yr), which includes smaller-scale crustal faults and realistic subduction zone geometries and considers earthquake cycle processes (Figure 3a). To highlight the difference between plate-motion models, such as MORVEL and the GBM, we compare model predicted velocities with the block rotation component of the predicted velocity (Figure 3b). GPS velocities at plate interiors are described well by the rotation component, while large discrepancies (residuals) between the model predictions and rotational component demonstrate the importance and spatial extent of earthquake strain accumulation due to slip-deficit rate.

The reference realization of the GBM was based on minimizing the residual velocity while maintaining consistency with geological observations on the rate and sense of fault slip noted in previous studies, contained in Table 1, and references therein. To this end, the constraints mentioned in the previous section were added. Ninety percent of the velocities used to constrain the model are fit to within 5 mm/year. While most residual vectors are randomly oriented, systematic misfits highlight areas in which fault geometries are misrepresented or a more complicated physical model may be necessary. These regions include Alaska, where likely a viscoelastic model is required to account for continued postseismic deformation following the 1964 Great Alaskan earthquake (e.g., Suito & Freymueller, 2009), Taiwan, the Philippines, and Indonesia (where there are frequent earthquakes, perhaps contaminating the interseismic signal, complicated fault geometries, and many submarine faults). Misfits to the model predictions in Greenland and northern Canada are likely due to glacial isostatic adjustment (e.g., Khan et al., 2016), while misfits on the Pacific Plate, except for Hawaiian stations, are likely influenced by slip-deficit rates on faults in the Southwest Pacific. The average residual here is ~ 3 mm/year, but it is possible that adding another block would improve model predictions. Zoomed in figures of residuals for three regions are provided in the supporting information, and full results are available in the Github repository.

Global slip-deficit rates range from ~ 1 to ~ 240 mm/year in both the dip-slip and strike-slip components, with the fastest rates located at or around the northern end of the Tonga subduction zone (Figures 4 and 5a). Slip-deficit rates predicted by the GBM across convergent margins with a TDE mesh (see Figure 2) are consistent with MORVEL relative plate motion estimates (DeMets et al., 2010) and those of previous studies (Table 1). Comparing the geographical distribution of fast (slip-deficit rate ≥ 20 mm/year) right-lateral to left-lateral faults, we see that apart from the Kunlun fault in Tibet, fast left-lateral faults are clustered in Indonesia and the Philippines. It is worth noting however that these rates are more poorly constrained due to limited station coverage and complex fault geometries. Fast right-lateral faults, on the other hand, have a much wider spatial distribution and we note that many of the world's well-known strike-slip faults are right-lateral, such as the San Andreas (USA), North Anatolian (Turkey), Alpine fault (New Zealand), and the Sumatra fault (shown in red in Figure 5b).

In the following sections, we compare GBM results to two previous regional studies as well as GSRM v2.1. Readers are directed to the Github repository to view complete model results and KML files to view figure graphics plotted on to the globe.

5.1. Comparison With Regional Models: Japan

We compare the results of GBM in Japan against the regional model by Loveless and Meade (JB1, 2010) and find that the two models are generally similar (fault slip deficit rates within ± 1 mm/year), particularly in Hokkaido, Shikoku, Kyushu, and the Ryukyu Islands. On the island of Honshu, however, there are a few differences. In GBM we note slightly faster convergence (~ 5 mm/year) off the west coast of northern Honshu, and off the west coast we observe a different pattern of slip partitioning on the roughly parallel faults of the Niigata-Kobe Tectonic Zone (NKTZ) and the Sea of Japan incipient subduction zone, with slower rates on the latter and slightly faster rates on the former. Slip-deficit rates along the southern portion of the NKTZ and Median Tectonic Line (MTL) are consistent with JB1; however, the rates on faults bounding small blocks between them have a different distribution. GBM left-lateral slip-deficit rates on the Itoigawa-Shizuoka

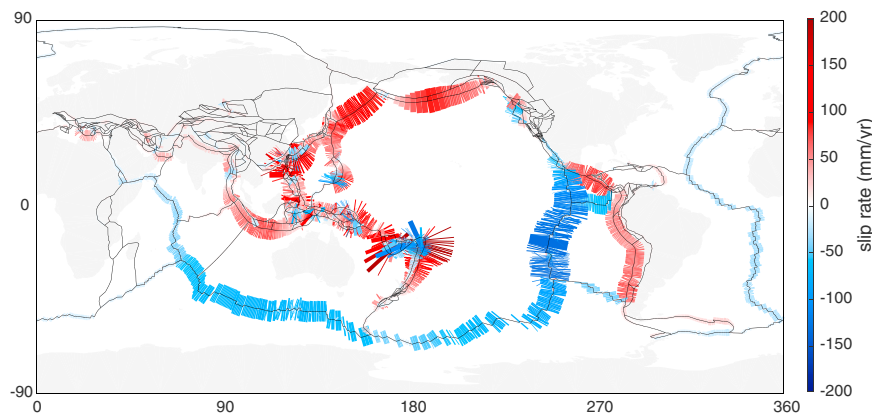


Figure 4. Model predicted dip-slip/tensile slip deficit rates (mm/year). Convergence is shown as positive and red. The color shade and width of the line indicate the magnitude of slip-deficit rate.

Tectonic Line, between the NKTZ and MTL are a few millimeters per year faster than in JB1 and thus slightly closer to paleoseismic rates. It is possible the high degree of similarity between JB1 and GBM is a result of JB1's inclusion of many of the surrounding tectonic plates (e.g. Amur, Okhotsk, Yangtze, Philippine Sea), which introduces into the regional model the major faults located at greater distances from Japan. Further, the data sets used in JB1 and the GSRM/GBM do include some overlap (Sagiya et al., 2000) but are not identical, with seven additional studies incorporated in the GBM velocity field.

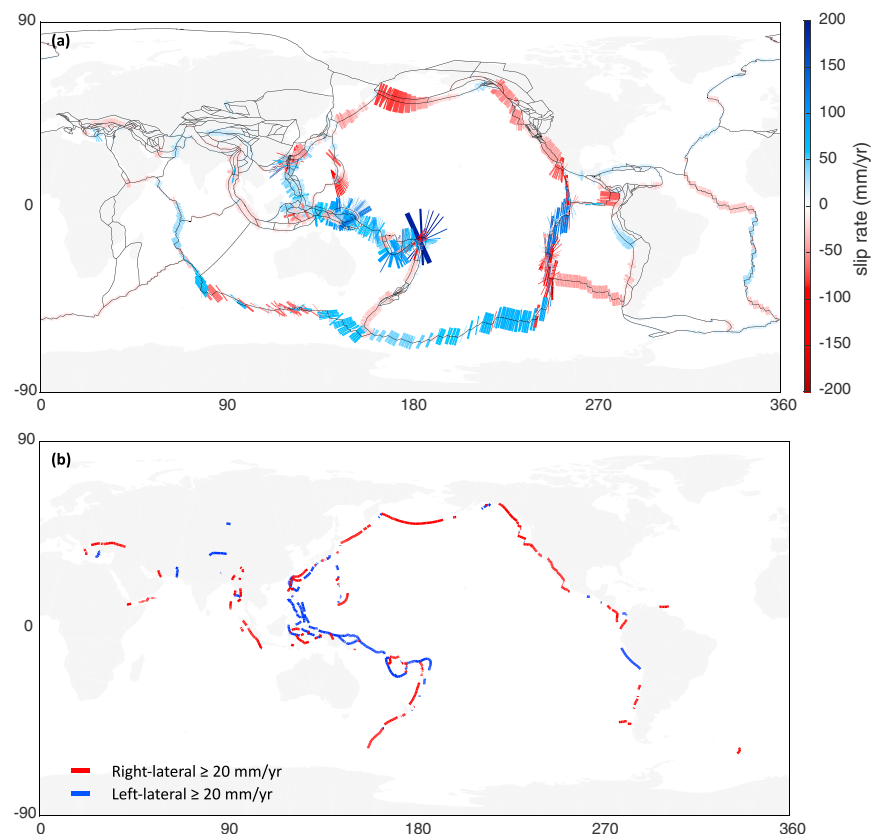


Figure 5. (a) Model predicted strike-slip deficit rates (mm/year). Right-lateral shown as red and left-lateral in blue. The color shade and width of the line indicate the magnitude of slip deficit rate. (b) Faults with strike-slip deficit rates of ≥ 20 mm/year.

Table 2
Euler Pole Location and Rate, Relative to the North America Plate, for Common Plates in GBM and GSRM

Plate name	GBM			GSRM		
	Pole lat (°)	Pole lon (°)	Rate (°/Myr)	Pole lat (°)	Pole lon (°)	Rate (°/Myr)
Africa	80.87	81.21	0.22	79.15	69.15	0.22
Amur	69.58	127.03	0.26	67.43	120.03	0.26
Antarctica	51.41	125.51	0.24	53.11	124.50	0.24
Arabia	49.07	29.15	0.54	52.17	23.77	0.47
Australia	27.15	52.59	0.75	26.96	52.95	0.76
Baja California	-50.42	105.01	0.77	-48.59	100.65	0.77
Bering	-59.47	9.26	0.21	-60.71	7.82	0.26
Caribbean	75.41	217.46	0.18	73.48	184.16	0.17
Cocos	28.96	229.99	1.14	30.81	226.62	1.03
Danakil	19.72	40.56	3.25	20.67	40.58	2.60
Eurasia	71.30	121.81	0.23	69.34	118.64	0.23
Gonave	4.67	108.31	0.29	40.84	274.02	0.28
India	44.37	42.41	0.67	48.80	29.76	0.53
Juan de Fuca*	-34.90	64.11	1.50	-32.27	67.39	1.14
Lwandle	79.51	76.69	0.22	65.01	53.36	0.23
Mariana	14.85	143.45	6.10	10.24	138.78	2.32
North Bismarck	-48.82	101.54	0.82	-26.68	128.70	1.36
Nazca	68.10	239.70	0.51	65.81	237.94	0.50
Okhotsk	5.13	355.97	0.03	61.93	123.46	0.10
Pacific	-49.69	108.61	0.78	-49.12	103.93	0.79
Puerto Rico	32.98	287.83	0.57	45.73	280.80	0.31
Philippine Sea	-41.97	338.75	1.06	-51.61	351.98	0.85
Rivera*	22.24	251.13	4.31	21.10	251.66	4.32
Rovuma	76.16	193.29	0.25	70.41	62.52	0.22
South America	-15.08	125.17	0.15	-14.77	123.65	0.15
South Bismarck	6.37	330.15	8.76	6.98	329.13	6.53
Scotia	-67.66	271.50	0.33	18.84	110.86	0.12
Sinai	55.74	35.24	0.36	49.70	35.51	0.49
Shetland	58.84	127.59	1.28	60.47	125.12	1.78
Somalia	80.12	75.69	0.23	79.99	196.62	0.25
Solomon Sea	22.59	44.37	0.83	-3.25	126.73	1.86
Sunda	73.79	235.96	0.24	83.31	174.69	0.26
Tonga	27.43	5.42	7.17	26.35	5.88	8.85
Victoria	33.41	34.29	0.42	71.79	188.65	0.24
Woodlark	15.85	92.01	0.92	-1.70	127.27	2.14
Yangtze	69.34	133.10	0.31	69.30	129.63	0.32

Note. * indicates plates with constrained rotation vectors in GBM. GBM = global block model; GSRM = Global Strain Rate Model.

5.2. Comparison With Regional Models: Aegean

We next compare GBM with the regional model for the Aegean from Vernant et al. (2014; V14), which does not include faults in Anatolia or northern Greece. Convergence rates of ~35 mm/year across the Hellenic subduction zone are consistent between GBM, V14, and Reilinger et al. (2006); however, these rates may be dependant on how the Aegean megathrust is modeled, as freely creeping or temporarily locked (e.g., Howe & Bird, 2010). No constraints are applied in GBM and slip-deficit rates across the TDEs indicate regions of locking and creep. We find improved fits to the data when the eastern boundary of the Western Peloponnese block in V14 is instead shifted eastward to the Argolikos Gulf fault. In the Corinth Gulf, GBM predicts 14 mm/year

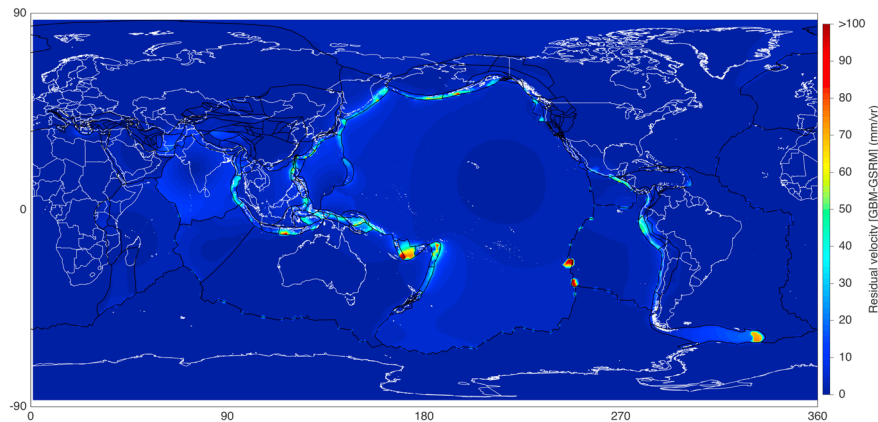


Figure 6. Residual differences between GBM and GSRM model predicted velocities across a 1° by 1° grid. Dark blue indicates 1 mm/year or less of difference between the two models. Hot colors indicate larger differences with the scale saturating at 100 mm/year. GBM = global block model; GSRM = Global Strain Rate Model.

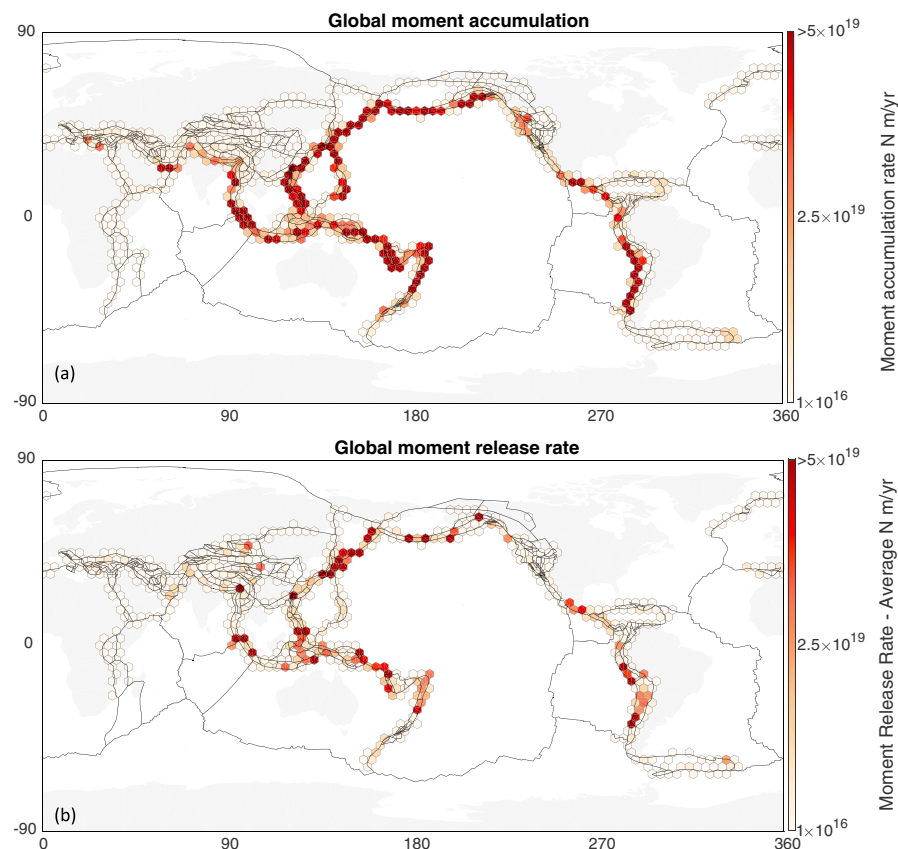


Figure 7. (a) The rate of seismic moment accumulation across globally distributed hexagon-shaped bins. Areas with no hexagon show regions with zero moment accumulation estimated by GBM. The earth is accumulating strain at a rate of 1.09×10^{22} N·m/year, based on fault geometries and slip-rates calculated by GBM. This calculation excludes strain accumulated at mid-ocean ridges, which is poorly resolved by the land-based geodetic observations. (b) The averaged rate of seismic moment release across the same hexagon bins as in (a). See text for a description of the earthquake catalog used. The total global rate of seismic moment release is 0.95×10^{22} N·m/year (excludes mid-ocean ridge events). GBM = global block model.

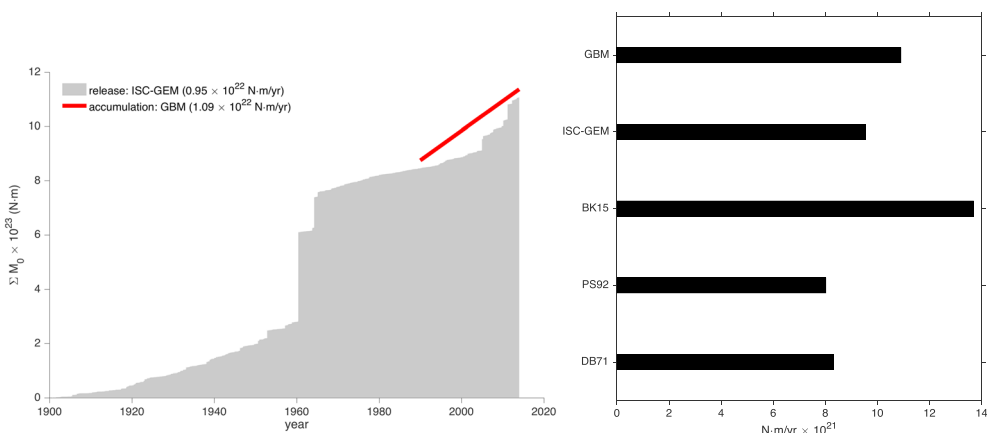


Figure 8. (Left) Cumulative moment release through time compared with the rate of moment accumulation calculated from GBM. (Right) Comparison of moment accumulation rate estimated with GBM against calculated moment release rates of Pacheco and Sykes (1992; PS92), Davies and Brune (1971; DB71), and the ISC-GEM catalog, as well as the SHIFT-GRSM model prediction of seismicity (Bird & Kreemer, 2015; BK15). GBM = global block model; GSRM = Global Strain Rate Model.

of extension versus 9 mm/year in V14; however, there is a systematic misfit in GBM across this boundary. On the NE-SW striking faults defining the Rhodes block (to the east of Crete surrounding the island of Rhodes) GBM predicts slightly faster slip deficit rates (~2 mm/year) in both the fault-normal and fault-parallel components of motion. V14 has a mean residual of 2.8 mm/year across 191 stations, while GBM has a mean residual of 2.35 mm/year for the subset of similar stations and 2.4 mm/year across the total 329 GPS velocities in the same region. The majority of the misfit in GBM is attributed to stations on either side of the Corinth Gulf.

5.3. Comparison With GSRM

The angular velocities and Euler pole locations of corresponding plates in GBM and GSRMv2.1 (Kreemer et al., 2014) are generally similar, with an average difference of $\sim 5^\circ$ in longitude and latitude of the pole location and $0.08^\circ/\text{Myr}$ in plate rotation rate (Table 2). Large differences occur between the Gonave, Lwandle, Okhotsk, Rovuma, Scotia, Solomon Sea, Sunda, Somalia, Victoria, and Woodlark plates (see the supporting information of Kreemer et al., 2014, for a map of plate locations). Differences could be a result of poor station coverage, additional data, or elastic deformation from earthquake cycle effects. We also compare predicted surface velocities from GBM and GSRMv2.1 across a grid of points with 1° by 1° spacing (Figure 6). We find a high degree of similarity between the two models with the largest exceptions at locations with known tectonic plates but without geodetic data to constrain them (e.g., the Sandwich and Galapagos plates). Other large discrepancies in regions such as Papua New Guinea, Central America, Peru, the Aleutians, and the Philippines are likely due to earthquake cycle effects (hot colors in Figure 6).

6. Global Moment Accumulation and Release

Geodetically constrained slip deficit rates (\dot{s}) from GBM can be used to estimate the global interseismic moment accumulation rate when combined with model fault areas (A), and an assumed shear modulus of 30 GPa (μ). The global moment accumulation rate ($\dot{M} = \mu A \dot{s}$) includes all continental faults and oceanic subduction zones but excludes mid-ocean ridges where data are too sparse to estimate interseismic coupling. We find a global moment accumulation rate of $1.09 \times 10^{22} \pm 0.08 \text{ N}\cdot\text{m}/\text{year}$, equivalent to one $M_W = 8.66$ earthquake per year (Figure 7a). Unsurprisingly, the highest moment accumulation rates are coincident with subduction zones and convergent margins, due to their large fault surface areas (Figure 7a).

To compare the rate of interseismic moment accumulation with the rate of coseismic moment release, we use the ISC-GEM catalog (Storchak et al., 2013), which includes all events $M_W \geq 5.5$ from 1900 to 2013. Averaged over the 113-year period and considered for all non-mid-ocean ridge events, the earth has released moment at a rate of $0.95 \times 10^{22} \text{ N}\cdot\text{m}/\text{year}$, equivalent to one $M_W = 8.62$ earthquake per year (Figure 7b). The global difference between the calculated moment accumulation rate and averaged moment release rate is $0.14 \times 10^{22} \text{ N}\cdot\text{m}/\text{year}$, equivalent to a $M_W = 8.06$ earthquake per year, where the estimated moment accumulation rate is 12% larger than the release rate. A larger value for the total moment accumulation rate versus

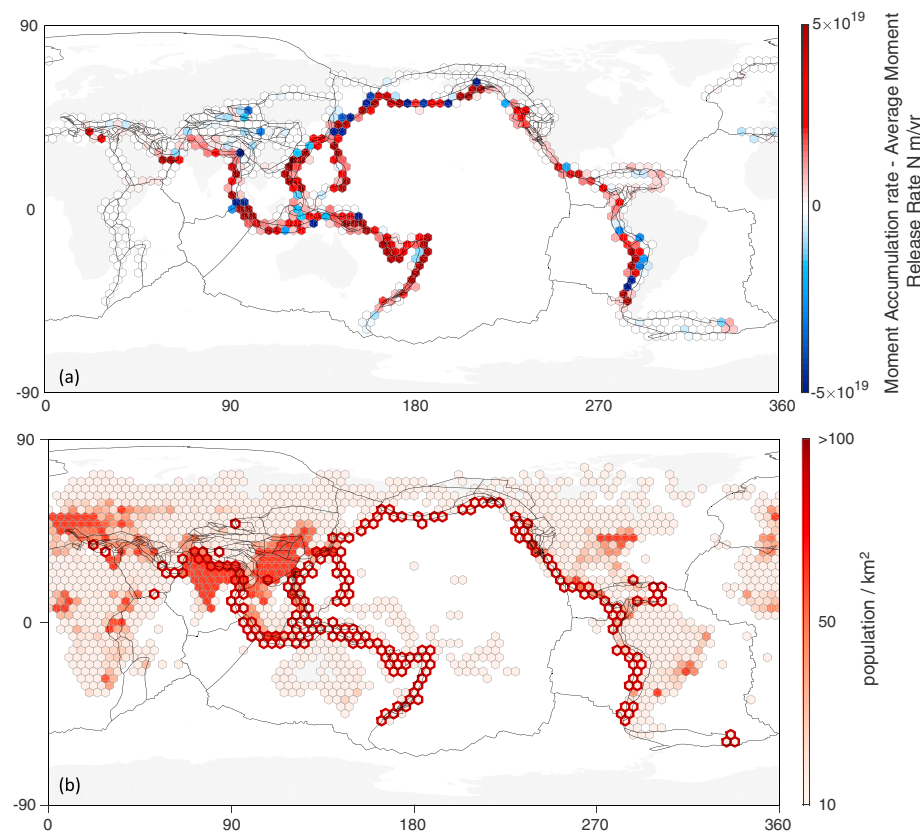


Figure 9. (a) The difference between estimated moment accumulation and averaged historic seismic moment released across the hexagon grid in Figure 7. Red shows an excess of moment accumulation, while blue shows regions that have historically released more strain than the present rate of accumulation. White shows regions in balance. The global difference is 0.14×10^{22} N·m/year. (b) Population density (per square kilometer, Center for International Earth Science Information Network—CIESIN—Columbia University, 2016). Bold outlined hexes show regions where there is an excess of moment accumulation $>5 \times 10^{18}$ N·m/year.

average release rate is not unexpected as this comparison assumes all moment to be released seismically, which is not the case (e.g., slow slip events).

Our calculation of average moment accumulation per year is within ~75% of previous moment release-rate calculations by Pacheco and Sykes (1992) and Davies and Brune (1971; Figure 8), computed from seismic events spanning 1900–1989 and 1897–1968, respectively. The seismic moment release estimate from the SHIFT-GSRM2f model is 25% higher, which may be a consequence of the model forecasting global earthquake rates for high magnitudes ($7.65 < M_W < 9.0$) at rates slightly above those in the Global CMT catalog (Bird & Kreemer, 2015). Comparing the rate of moment accumulation against the historical record of cumulative moment release (Figure 8), we find that while the rate of moment accumulation is close to the averaged rate of release, there are many periods with a lower rate of moment release. For instance, the recent moment accumulation rate (Figure 8) is 4 times higher than the moment release from 1920 to 1950. The disparity between decadal rates and the overall average moment balance highlights the importance of regional comparisons and the consideration of great earthquakes with long recurrence intervals.

In order to compare the geodetically constrained moment accumulation with the historic averaged rate of release on a regional basis, we construct a grid of hexagonal bins and sum the moment rates within each. We find that many areas are accumulating moment at a rate faster than the historic release rate over the past 113 years (Figure 9a). These regions (red in Figure 9a) are thus likely to experience more seismic activity in the future than regions appearing in blue, which indicates an area where more moment has been released than accumulated. However, it is important to note that all of the accumulated moment may not be released seismically. There are regions marked by a combination of areas with greater moment accumulation and greater release, implying that portions of the fault will experience greater seismicity in the nearer future.

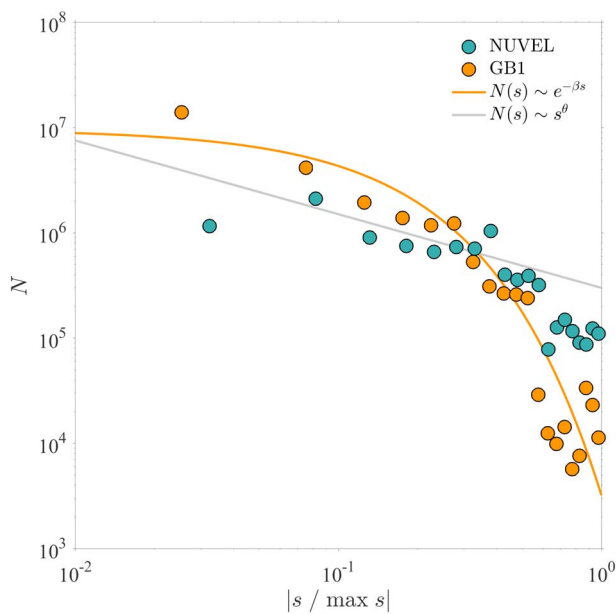


Figure 10. Frequency distribution of fault slip rates, \dot{s} , from a model with NUVEL (14 blocks) plate boundaries and no strain accumulation (dark green circles) and the global block model GBM (307 blocks, orange circles). In both cases the greatest fraction of fault system length is at slow slip rates while there is relatively little fault system length near the fastest slip rates. The GBM frequency distribution is not well represented by a power law, $N(\dot{s}) \sim \dot{s}^\theta$, (solid gray line), suggested by Meade (2007). Instead, the GBM frequency distribution is better described by an exponential distribution, $N(\dot{s}) \sim e^{-\beta\dot{s}}$, with $\beta \approx 8$.

NUVEL model geometry (DeMets et al., 1990), that does not include any small scale faults can also be described by an exponential function (Figure 10). In contrast, Meade (2007) showed that the frequency distribution of slip-deficit rates in southern California could be fit by a power law distribution, $N(\dot{s}) \sim \dot{s}^\theta$, where $\theta \approx -0.75$ (gray line in Figure 10). However, this power-law form of the slip-rate frequency distribution does not describe the global data as it does not fall off quickly enough at fast slip-deficit rates (Figure 10). Relative to the $\theta = -0.7$ power-law distribution, the exponential distribution falls off more quickly and indicates that fastest slip rates contribute less to overall fault system activity. This discrepancy may result from the limited range of fault slip deficit rates in California (Meade, 2007) versus the wider range of rates globally.

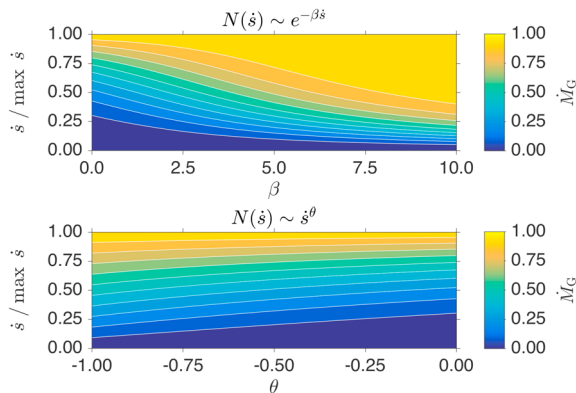


Figure 11. Cumulative moment accumulation rates. The exponential distribution case is shown in the upper panel and is the case relevant to the slip rate distribution inferred from global block model. The horizontal axis is the exponential distribution parameter β and the normalized slip rate $\dot{s}/\max\dot{s}$. For the global block model we find $\beta \approx 8.0$. The minimum resolved slip rate in the global block model ≈ 3.0 mm/year and the fastest slip rate is ≈ 200 mm/year so that the resolved normalized resolved slip rate is 0.015, which implies that the global block model resolves 98% of the global moment accumulation rate. The power-law case from a previous local southern California study (Meade, 2007) is shown in the lower panel for reference.

Examples include Valdivia (Chile), Maule (Chile), Sumatra, and Tohoku (Japan) where great earthquakes have occurred during the past 113 years (1960 $M_W = 9.5$, 2010 $M_W = 8.8$, 2004 $M_W = 9.0$, and 2011 $M_W = 9.0$, respectively). Comparing these results with human population density (Figure 9b) indicates large moment accumulation disparity (accumulation minus release $\geq 5 \times 10^{18}$ N·m/year) occurs in densely populated regions in Japan, China, Indonesia, California, and the entire Himalayan range front (bold outlined hexagons with dark red fill Figure 9b). Furthermore, we find that 49.3% of the world's population lives within 200 km of an active fault with slip-deficit rates of 2 mm/year or greater.

7. Quantifying the Missing Contribution to Moment Accumulation Rate Estimates

The frequency distribution of fault slip deficit rates can provide a statistical description of the spatial partitioning of deformation in the crust, and enable quantification of the fraction of fault system with a particular slip-deficit rate (Meade, 2007). In the following, we analyze the frequency distribution of fault slip-deficit rates globally based on the results from GBM. Each fault is first divided into 1-km-long segments, assigning the same slip-deficit rate as the original fault to each segment, thus homogenizing all fault segment lengths in the GBM. The distribution of fault length at a given slip-deficit rate illustrates that only 17.5% of the total fault length (446,870 km) have slip-deficit rates greater than 50 mm/year, and 31% less than 5 mm/year (Figure 10). We find that an exponential distribution provides the most accurate description of the slip-deficit rate frequency distribution, $N(\dot{s}) \sim e^{-\beta\dot{s}}$ (Figure 10). For comparison, the fault slip-deficit rate frequency distribution of a 12-plate model, based on the

empirically constrained exponential fault slip-rate distribution can be used to determine the total amount of deformation accommodated by faults at given slip-deficit rate (Meade, 2007). To find the geometric moment rate per unit length, \dot{M}_G , we integrate the length of the fault system at a given slip-deficit rate by the slip-deficit rate, $\dot{M}_G = \int_0^{\dot{s}_{\max}} N(\dot{s})\dot{s}d\dot{s}$, to obtain,

$$\dot{M}_G = \frac{1 - e^{-\beta\dot{s}}(\beta\dot{s} + 1)}{1 - e^{-\beta}(\beta + 1)} \quad (1)$$

We estimate $\beta \approx 0.13$ with the global distribution of fault slip deficit rates determined by GBM. The minimum resolved slip rate, \dot{s} , in the GBM is ~ 3 mm/year and the fastest slip rate is ~ 200 mm/year; therefore, the smallest normalized resolved slip rate, $\dot{s}_{\text{norm}} = |\dot{s}_{\text{obs}}/\dot{s}_{\max}|$ (where \dot{s}_{\max} is the maximum slip-rate in the fault system), is 0.015. This implies that the GBM accounts for 98% of the global moment accumulation rate (Figure 11). Faults with very slow slip rates (< 1 mm/year) are likely underrepresented in GBM, since they are difficult to model geodetically. Thus, motion due to

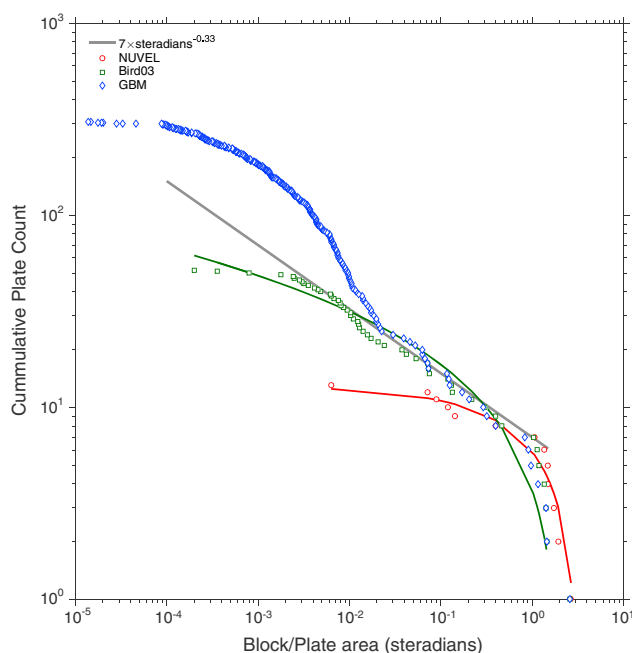


Figure 12. Plate area versus total number of plates exceeding that area for GBM (blue), Bird (2003, green), and NUVEL (red). Power law relationship suggested by Bird (2003) is shown by the gray solid line. Green and red solid lines show power law fits to Bird (2003) and NUVEL data, respectively. GBM = global block model.

such faults may be artificially mapped on to other structures (McCaffrey, 2005; Meade & Hager, 2005). Further, regions with sparse or nonexistent geodetic networks are likely missing active faults in GBM.

8. Frequency Distribution of Tectonic Plate Size

As the number of tectonic plates has increased from 12 (e.g., NUVEL; DeMets et al., 1990) to 52 (Bird, 2003), the natural questions are as follows: How many plates remain to be discovered, and how many are necessary to explain geodetically observed deformation? We find that a GBM with 307 blocks fits the observed global GPS velocities with a mean residual magnitude of 2.2 mm/year, and the frequency distribution of plate areas appears consistent with previous models (NUVEL and Bird, 2003). While a power law well described the frequency distribution of plate areas for areas between 0.002 and 1 steradian in the Bird (2003) model (Figure 12), there are many more small blocks in GBM and this approximation instead only seems valid for plate areas between 0.02 and 1 steradian. All three models show a flattening out as the smallest areas within the model are approached; for GBM this occurs at 9×10^{-5} steradians, as opposed to 0.07 and 0.002 steradians for NUVEL and Bird (2003), respectively (Figure 12). Bird (2003) attributed this to model incompleteness, suggesting the existence of small blocks not yet resolved. A future step would be to apply the total variation regularization algorithm of Evans et al. (2015) to determine the simplest arrangement of blocks to fit the geodetic observations at a given resolution. Reducing the number of blocks, while maintaining a good fit to the data would allow for the determination of the Earth's most seismically hazardous faults. This simplest number of blocks to still fit the data may follow the Bird (2003) power law more closely.

9. Conclusions

Acknowledgments

A portion of this material is based on data provided by the Continuously Operating Caribbean GPS Observational Network (COCONet) operated by UNAVCO for EarthScope (www.earthscope.org) and supported by the National Science Foundation (EAR-1042906/9). All sources for the data used are listed in the references and tables. The authors wish to thank Laura Wallace for generously providing New Zealand GPS velocities and block model geometries for New Zealand, Tonga/Vanuatu, and Papua New Guinea. We also wish to thank Andrea Walpersdorf for generously providing her Iran block model geometry. A great thanks to Corné Kreemer for sharing the global velocity field from GSRMv2.1. The authors wish to thank Jeff Freymueller, Peter Bird, and an anonymous reviewer for their helpful comments and suggestions, which helped to strengthen this manuscript. Model input/output files and KML-format output files can be found at https://github.com/brendanjmeade/reference_gbm and the Blocks software at <https://github.com/jploveless/Blocks>.

Geodetic observations of motion at the Earth's surface reveal the complex interplay between long-term tectonic motions and short-term earthquake cycle processes. Here we describe a block model that integrates these two processes across the globe. The reference GBM features 307 blocks, comprised of 446,870 km of fault trace, and explains interseismic GPS observations from 19,664 worldwide GPS stations at 2.2-mm/year resolution. We find general agreement with previous slip and slip-deficit rate estimates, with some differences potentially resulting from the interactions with faults in neighboring regions. Slip-deficit rates from the reference GBM are consistent with an exponential frequency distribution and yield a bound on the percentage of missing interseismic strain accumulation from the reference GBM. These estimates suggest that if all faults with slip rates greater than 3 mm/year are accurately mapped, they will account for 98% of the world's moment accumulation. We suggest that the vague question of "How many tectonic plates are there?" can be replaced with the more well-posed question, "What is the frequency distribution of plate sizes and fault slip rates necessary to describe crustal motions at a given level of resolution?", which allows for different models to be meaningfully compared and tested.

The GBM moment accumulation rate, 1.09×10^{22} N·m/year, is equivalent to a $M_W = 8.66$ earthquake per year, while the average yearly release as determined from historic seismicity (1900–2013) is 0.95×10^{22} N·m/year. Although these scalar rates agree within 12%, regionally there are large differences between accumulation and release. For example, portions of the Sumatran and Chilean subduction zones are in balance/deficit while others, such as the Cascadia subduction zone, have stored more energy than has been released and thus pose a greater seismic risk.

References

- Aktug, B., Dikmen, U., Dogru, A., & Ozener, H. (2013). Seismicity and strain accumulation around Karliova Triple Junction (Turkey). *Journal of Geodynamics*, 67, 21–29. <https://doi.org/10.1016/j.jog.2012.04.008>
- Aktug, B., Dogru, A., Ozener, H., & Peyret, M. (2015). Slip rates and locking depth variation along central and easternmost segments of North Anatolian Fault. *Geophysical Journal International*, 202(3), 2133–2149. <https://doi.org/10.1093/gji/ggv274>

- Aktug, B., & Kilicoglu, A. (2006). Recent crustal deformation of Izmir, Western Anatolia and surrounding regions as deduced from repeated GPS measurements and strain field. *Journal of Geodynamics*, 41(5), 471–484.
- Aktug, B., Meherremov, E., Kurt, M., Özdemir, S., Esedov, N., & Lenk, O. (2013). GPS constraints on the deformation of Azerbaijan and surrounding regions. *Journal of Geodynamics*, 67, 40–45.
- Aktug, B., Nocquet, J. M., Cingöz, a., Parsons, B., Erkan, Y., England, P., et al. (2009). Deformation of western Turkey from a combination of permanent and campaign GPS data: Limits to block-like behavior. *Journal of Geophysical Research*, 114, B10404. <https://doi.org/10.1029/2008JB006000>
- Argus, D. F., Gordon, R. G., & DeMets, C. (2011). Geologically current motion of 56 plates relative to the no-net-rotation reference frame. *Geochemistry, Geophysics, Geosystems*, 12, Q11001. <https://doi.org/10.1029/2011GC003751>
- Audemard, F. A., Machette, M. N., Cox, J. W., Dart, R. L., & Haller, K. M. (2000). Map and database of Quaternary faults in Venezuela and its offshore regions (US Geological Survey Open-File Report, 00-0018).
- Baldwin, S. L., Fitzgerald, P. G., & Webb, L. E. (2012). Tectonics of the New Guinea region. *Annual Review of Earth and Planetary Sciences*, 40, 495–520.
- Battaglia, M., Murray, M. H., Serpelloni, E., & Bürgmann, R. (2004). The Adriatic region: An independent microplate within the Africa-Eurasia collision zone. *Geophysical Research Letters*, 31, L09605. <https://doi.org/10.1029/2004GL019723>
- Bayer, R., Chery, J., Tatar, M., Vernant, P., Abbassi, M., Masson, F., et al. (2006). Active deformation in Zagros-Makran transition zone inferred from GPS measurements. *Geophysical Journal International*, 165(1), 373–381. <https://doi.org/10.1111/j.1365-246X.2006.02879.x>
- Bennett, R. A., Spinler, J. C., Compton, K., Rockwell, T. K., & Gath, E. (2014). Global positioning system constraints on active crustal deformation in central Panamá. *Seismological Research Letters*, 85(2), 278–283.
- Bilham, R., Larson, K., & Freymueller, J. (1997). GPS measurements of present-day convergence across the Nepal Himalaya. *Nature*, 386, 61–64.
- Bird, P. (2003). An updated digital model of plate boundaries. *Geochemistry, Geophysics, Geosystems*, 4(3), 1027. <https://doi.org/10.1029/2001GC000252>
- Bird, P. (2009). Long-term fault slip rates, distributed deformation rates, and forecast of seismicity in the western United States from joint fitting of community geologic, geodetic, and stress direction data sets. *Journal of Geophysical Research*, 114, B11403. <https://doi.org/10.1029/2009JB006317>
- Bird, P., & Kreemer, C. (2015). Revised tectonic forecast of global shallow seismicity based on version 2.1 of the Global Strain Rate Map. *Bulletin of the Seismological Society of America*, 105(1), 152–166.
- Bird, P., & Liu, Z. (2007). Seismic hazard inferred from tectonics: California. *Seismological Research Letters*, 78(1), 37–48.
- Center for International Earth Science Information Network—CIESIN—Columbia University (2016). Gridded Population of the World, Version 4 (GPWv4): Population Count.
- Chase, C. G. (1978). Plate kinematics: The Americas, East Africa, and the rest of the world. *Earth and Planetary Science Letters*, 37(3), 355–368. [https://doi.org/10.1016/0012-821X\(78\)90051-1](https://doi.org/10.1016/0012-821X(78)90051-1)
- Ching, K. E., Rau, R. J., Johnson, K. M., Lee, J. C., & Hu, J. C. (2011). Present-day kinematics of active mountain building in Taiwan from GPS observations during 1995–2005. *Journal of Geophysical Research*, 116, B09405. <https://doi.org/10.1029/2010JB008058>
- Chlieh, M., Avouac, J. P., Sieh, K., Natawidjaja, D. H., & Galetzka, J. (2008). Heterogeneous coupling of the Sumatran megathrust constrained by geodetic and paleogeodetic measurements. *Journal of Geophysical Research*, 113, B05305. <https://doi.org/10.1029/2007JB004981>
- Chlieh, M., Mothes, P. A., Nocquet, J.-M., Jarrin, P., Charvis, P., Cisneros, D., et al. (2014). Distribution of discrete seismic asperities and aseismic slip along the Ecuadorian megathrust. *Earth and Planetary Science Letters*, 400, 292–301. <https://doi.org/10.1016/j.epsl.2014.05.027>
- DISS Working Group (2010). Database of individual seismogenic sources (DISS), in: Version 3.1. 1: A compilation of potential sources for earthquakes larger than M5.5 in Italy and surrounding areas: Available from the Istituto Nazionale di Geofisica e Vulcanologia (INGV) at <http://diss.ingv.it/dissNet/>, <https://doi.org/10.6092/INGV.IT-DISS3.2.0>
- Davies, G. F., & Brune, J. N. (1971). Regional and global fault slip rates from seismicity. *Nature*, 229(4), 101–107.
- DeMets, C., Gordon, R. G., & Argus, D. F. (2010). Geologically current plate motions. *Geophysical Journal International*, 181(1), 1–80. <https://doi.org/10.1111/j.1365-246X.2009.04491.x>
- DeMets, C., Gordon, R. G., Argus, D. F., & Stein, S. (1990). Current plate motions. *Geophysical Journal International*, 101(2), 425–478. <https://doi.org/10.1111/j.1365-246X.1990.tb06579.x>
- DeShon, H., Engdahl, E. R., Thruber, C. H., & Brudzinski, M. (2005). Constraining the boundary between the Sunda and Andaman subduction systems: Evidence from the 2002 Mw 7.3 Northern Sumatra earthquake and aftershock relocations of the 2004 and 2005 great earthquakes. *Geophysical Research Letters*, 32, L24307. <https://doi.org/10.1029/2005GL024188>
- DeVries, P. M. R., Krastev, P. G., Dolan, J. F., & Meade, B. J. (2017). Viscoelastic block models of the North Anatolian Fault: A unified earthquake cycle representation of pre- and postseismic geodetic observations. *Bulletin of the Seismological Society of America*, 107(1), 403–417.
- Djamour, Y., Vernant, P., Bayer, R., Nankali, H. R., Ritz, J. F., Hinderer, J., et al. (2010). GPS and gravity constraints on continental deformation in the Alborz mountain range, Iran. *Geophysical Journal International*, 183(3), 1287–1301. <https://doi.org/10.1111/j.1365-246X.2010.04811.x>
- Djamour, Y., Vernant, P., Nankali, H. R., & Tavakoli, F. (2011). NW Iran-eastern Turkey present-day kinematics: Results from the Iranian permanent GPS network. *Earth and Planetary Science Letters*, 307(1–2), 27–34. <https://doi.org/10.1016/j.epsl.2011.04.029>
- Eguez, A., Alvarado, A., Yépez, H., Machette, M. N., Costa, C., Dart, R. L., & Bradley, L. A. (2003). Database and map of Quaternary faults and folds of Ecuador and its offshore regions (US Geological Survey Open-File Report, 03-289).
- Elliott, J., Freymueller, J. T., & Larsen, C. F. (2013). Active tectonics of the St. Elias orogen, Alaska, observed with GPS measurements. *Journal of Geophysical Research: Solid Earth*, 118, 5625–5642. <https://doi.org/10.1002/jgrb.50341>
- Evans, E. L., Loveless, J. P., & Meade, B. J. (2015). Total variation regularization of geodetically and geologically constrained block models for the Western United States. *Geophysical Journal International*, 202(2), 713–727.
- Feigl, K. L., Agnew, D. C., Bock, Y., Dong, D., Donnellan, A., Hager, B. H., et al. (1993). Space geodetic measurement of crustal deformation in central and southern California, 1984–1992. *Journal of Geophysical Research*, 98(B12), 21,677–21,712. <https://doi.org/10.1029/93JB02405>
- Galgana, G. A. (2009). Geodetic investigations of active crustal deformation in the Philippine plate boundary zone and the intraplate region of the central United States (PhD Dissertation). Department of Geological Sciences, Indiana University Bloomington.
- Hayes, G. P., Wald, D. J., & Johnson, R. L. (2012). Slab1.0: A three-dimensional model of global subduction zone geometries. *Journal of Geophysical Research*, 117, B01302. <https://doi.org/10.1029/2011JB008524>
- Hollingsworth, J., Jackson, J., Walker, R., & Nazari, H. (2008). Extrusion tectonics and subduction in the eastern South Caspian region since 10 Ma. *The Geological Society of America*, 36(10), 763–766. <https://doi.org/10.1130/G25008A.1>
- Howe, T. M., & Bird, P. (2010). Exploratory models of long-term crustal flow and resulting seismicity across the Alpine–Aegean orogen. *Tectonics*, 29, TC4023. <https://doi.org/10.1029/2009TC002565>

- Hubbard, J., Almeida, R., Foster, A., Sapkota, S. N., Bürgi, P., & Tappognon, P. (2016). Structural segmentation controlled the 2015 Mw 7.8 Gorkha earthquake rupture in Nepal. *Geology*, 44(8), 639–642.
- Jouanne, F., Mugnier, J. L., Gamond, J. F., Le Fort, P., Pandey, M. R., Bollinger, L., et al. (2004). Current shortening across the Himalayas of Nepal. *Geophysical Journal International*, 157(1), 1–14. <https://doi.org/10.1111/j.1365-246X.2004.02180.x>
- Karakhanian, A., Vernant, P., Doerflinger, E., Avagyan, A., Philip, H., Aslanyan, R., et al. (2013). GPS constraints on continental deformation in the Armenian region and Lesser Caucasus. *Tectonophysics*, 592, 39–45. <https://doi.org/10.1016/j.tecto.2013.02.002>
- Khan, S. A., Sasgen, I., Bevis, M., van Dam, T., Bamber, J. L., Wahr, J., et al. (2016). Geodetic measurements reveal similarities between post-Last Glacial Maximum and present-day mass loss from the Greenland ice sheet. *Science advances*, 2(9), e1600931.
- Kobayashi, D., LaFemina, P., Geirsson, H., Chichaco, E., Abrego, A. A., Mora, H., & Camacho, E. (2014). Kinematics of the western Caribbean: Collision of the Cocos Ridge and upper plate deformation. *Geochemistry, Geophysics, Geosystems*, 15, 1671–1683. <https://doi.org/10.1029/2014GC005234>
- Koons, P. O., Hooks, B. P., Pavlis, T., Upton, P., & Barker, A. D. (2010). Three-dimensional mechanics of Yakutat convergence in the southern Alaskan plate corner. *Tectonics*, 29, TC4008. <https://doi.org/10.1029/2009TC002463>
- Koulali, A., Ouazar, D., Tahayt, A., King, R. W., Vernant, P., Reilinger, R. E., et al. (2011). New GPS constraints on active deformation along the Africa—Iberia plate boundary. *Earth and Planetary Science Letters*, 308(1–2), 211–217. <https://doi.org/10.1016/j.epsl.2011.05.048>
- Koulali, A., Susilo, S., McClusky, S., Meilano, I., Cummins, P., Tregoning, P., et al. (2016). Crustal strain partitioning and the associated earthquake hazard in the eastern Sunda-Banda Arc. *Geophysical Research Letters*, 43, 1943–1949. <https://doi.org/10.1002/2016GL067941>
- Kreemer, C., Blewitt, G., & Klein, E. C. (2014). A geodetic plate motion and Global Strain Rate Model. *Geochemistry, Geophysics, Geosystems*, 15, 3849–3889. <https://doi.org/10.1029/2014GC005407>
- Kreemer, C., Holt, W. E., Goes, S., & Govers, R. (2000). Active deformation in eastern Indonesia and the Philippines from GPS and seismicity data. *Journal of Geophysical Research*, 105(B1), 663–680.
- Kundu, B., & Gahalaut, V. K. (2013). Tectonic geodesy revealing geodynamic complexity of the Indo-Burmese arc region, North East India. *Current Science*, 104, 920–933.
- Lanza, J. C. V. (2014). Earthquake cycle and continental deformation along the Peruvian subduction zone (PhD thesis).
- Le Beon, M., Klinger, Y., Amrat, A. Q., Agnon, A., Dorbath, L., Baer, G., et al. (2008). Slip rate and locking depth from GPS profiles across the southern Dead Sea Transform. *Journal of Geophysical Research*, 113, B11403. <https://doi.org/10.1029/2007JB005280>
- Le Pichon, X. (1968). Sea-floor spreading and continental drift. *Journal of Geophysical Research*, 73(12), 3661–3697. <https://doi.org/10.1029/JB073i012p03661>
- Li, S., Freymueller, J., & McCaffrey, R. (2016). Slow slip events and time dependent variations in locking beneath Lower Cook Inlet of the Alaska-Aleutian subduction zone. *Journal of Geophysical Research: Solid Earth*, 121, 1060–1079. <https://doi.org/10.1002/2015jb012491>
- Loveless, J. P., & Meade, B. J. (2010). Geodetic imaging of plate motions, slip rates, and partitioning of deformation in Japan. *Journal of Geophysical Research*, 115, B02410. <https://doi.org/10.1029/2008JB006248>
- Loveless, J. P., & Meade, B. J. (2011a). Partitioning of localized and diffuse deformation in the Tibetan Plateau from joint inversions of geologic and geodetic observations TS AT. *Earth and Planetary Science Letters*, 303(1–2), 11–24. <https://doi.org/10.1016/j.epsl.2010.12.014>
- Loveless, J. P., & Meade, B. J. (2011b). Stress modulation on the San Andreas fault by interseismic fault system interactions. *Geology*, 39(11), 1035–1038. <https://doi.org/10.1130/G32215.1>
- Machare, J., Fenton, C. H., Machette, M. N., Lavenu, A., Costa, C., & Dart, R. L. (2003). Database and map of Quaternary faults and folds in Peru and its offshore region (US Geological Survey Open-File Report 2003-451).
- McCaffrey, R. (2005). Block kinematics of the Pacific-North America plate boundary in the southwestern United States from inversion of GPS, seismological, and geologic data. *Journal of Geophysical Research*, 110, B07401. <https://doi.org/10.1029/2004JB003307>
- McCaffrey, R. (2009). The tectonic framework of the Sumatra subduction zone. *Annual Review of Earth and Planetary Sciences*, 37, 345–366.
- McCaffrey, R., King, R. W., Payne, S. J., & Lancaster, M. (2013). Active tectonics of northwestern U.S. inferred from GPS-derived surface velocities. *Journal of Geophysical Research: Solid Earth*, 118, 709–723. <https://doi.org/10.1029/2012JB009473>
- McCaffrey, R., Qamar, A. I., King, R. W., Wells, R., Khazaradze, G., Williams, C. A., et al. (2007). Fault locking, block rotation and crustal deformation in the Pacific Northwest. *Geophysical Journal International*, 169(3), 1315–1340. <https://doi.org/10.1111/j.1365-246X.2007.03371.x>
- McClusky, S., Reilinger, R., Ogubazghi, G., Amleson, A., Healeb, B., Vernant, P., et al. (2010). Kinematics of the southern Red Sea–Afar Triple Junction and implications for plate dynamics. *Geophysical Research Letters*, 37, L05301. <https://doi.org/10.1029/2009GL041127>
- Meade, B. J. (2007). Power-law distribution of fault slip-rates in southern California. *Geophysical Research Letters*, 34, L23307. <https://doi.org/10.1029/2007GL031454>
- Meade, B. J., & Hager, B. H. (2005). Block models of crustal motion in southern California constrained by GPS measurements. *Journal of Geophysical Research*, 110, B03403. <https://doi.org/10.1029/2004JB003209>
- Meade, B. J., & Loveless, J. P. (2009). Block modeling with connected fault-network geometries and a linear elastic coupling estimator in spherical coordinates. *Bulletin of the Seismological Society of America*, 99(6), 3124–3139. <https://doi.org/10.1785/0120090088>
- Metzger, S., Jonsson, S., Nielsen, G., Hreinsdóttir, S., Jouanne, F., Giardini, D., & Villemain, T. (2013). Present kinematics of the Tjornes Fracture Zone, North Iceland, from campaign and continuous GPS measurements. *Geophysical Journal International*, 192(2), 441–455. <https://doi.org/10.1093/gji/ggs032>
- Métois, M., Vigny, C., Socquet, A., Delorme, A., Morvan, S., Ortega, I., & Valderas-Bermejo, C.-M. (2013). GPS-derived interseismic coupling on the subduction and seismic hazards in the Atacama region, Chile. *Geophysical Journal International*, 196(2), 644–655. <https://doi.org/10.1093/gji/ggt418>
- Michel, G. W., Becker, M., Reigber, C., Tibi, R., Yu, Y. Q., Zhu, S. Y., & Sea, P. (2001). Regional GPS data confirms highly accumulated strains prior to the Mw: 7.8 earthquake of June 4, 2000 at SE Sumatra. *Geophysical Journal International*, 146(3), 571–582.
- Minster, J. B., & Jordan, T. H. (1978). Present-day plate motions. *Journal of Geophysical Research*, 83(B11), 5331–5354. <https://doi.org/10.1029/JB083iB11p05331>
- Moreno, M., Melnick, D., Rosenau, M., Bolte, J., Klotz, J., Echtler, H., et al. (2011). Others Heterogeneous plate locking in the South–Central Chile subduction zone: Building up the next great earthquake. *Earth and Planetary Science Letters*, 305(3), 413–424.
- Morgan, W. J. (1968). Rises, trenches, great faults, and crustal blocks. *Journal of Geophysical Research*, 73(6), 1959–1982. <https://doi.org/10.1029/JB073i006p01959>
- Mousavi, Z., Walpersdorf, A., Walker, R., Tavakoli, F., Pathier, E., Nankali, H., et al. (2013). Global Positioning System constraints on the active tectonics of NE Iran and the South Caspian region. *Earth and Planetary Science Letters*, 377–378, 287–298. <https://doi.org/10.1016/j.epsl.2013.07.007>

- Mukti, M. M., Singh, S. C., Deighton, I., Hananto, N. D., Moeremans, R., & Permana, H. (2012). Structural evolution of backthrusting in the Mentawai Fault Zone, offshore Sumatran forearc. *Geochemistry, Geophysics, Geosystems*, 13, Q12006. <https://doi.org/10.1029/2012GC004199>
- Nocquet, J.-M., Chlieh, M., Mothes, P. A., Rolandone, F., Jarrin, P., Cisneros, D., et al. (2014). Motion of continental slivers and creeping subduction in the northern Andes. *Nature Geoscience*, 7, 287–291. <https://doi.org/10.1038/NGEO2099>
- Ozener, H., Arpat, E., Ergintav, S., Dogru, A., Cakmak, R., Turgut, B., & Dogan, U. (2010). Kinematics of the eastern part of the North Anatolian Fault Zone. *Journal of geodynamics*, 49(3), 141–150.
- Pacheco, J. F., & Sykes, L. R. (1992). Seismic moment catalog of large shallow earthquakes, 1900 to 1989. *Bulletin of the Seismological Society of America*, 82(3), 1306–1349.
- Peyret, M., Djambour, Y., Hessami, K., Regard, V., Bellier, O., Vernant, P., et al. (2009). Present-day strain distribution across the Minab-Zendan-Palami fault system from dense GPS transects. *Geophysical Journal International*, 179(2), 751–762. <https://doi.org/10.1111/j.1365-246X.2009.04321.x>
- Power, W., Wallace, L., Wang, X., & Reyners, M. (2012). Tsunami hazard posed to New Zealand by the Kermadec and southern New Hebrides subduction margins: An assessment based on plate boundary kinematics, interseismic coupling, and historical seismicity. *Pure and applied geophysics*, 169(1–2), 1–36.
- Radiguet, M., Cotton, F., Vergnolle, M., Campillo, M., Walpersdorf, A., Cotte, N., & Kostoglodov, V. (2012). Slow slip events and strain accumulation in the Guerrero gap, Mexico. *Journal of Geophysical Research*, 117, B04305. <https://doi.org/10.1029/2011JB008801>
- Rangin, C., Maurin, T., & Masson, F. (2013). Combined effects of Eurasia/Sunda oblique convergence and East-Tibetan crustal flow on the active tectonics of Burma. *Journal of Asian Earth Sciences*, 76, 185–194.
- Reilinger, R., McClusky, S., Vernant, P., Lawrence, S., Ergintav, S., Cakmak, R., et al. (2006). GPS constraints on continental deformation in the Africa-Arabia-Eurasia continental collision zone and implications for the dynamics of plate interactions. *Journal of Geophysical Research*, 111, B05411. <https://doi.org/10.1029/2005JB004051>
- Reilinger, R., McClusky, S., Paradissis, D., Ergintav, S., & Vernant, P. (2010). Tectonophysics geodetic constraints on the tectonic evolution of the Aegean region and strain accumulation along the Hellenic subduction zone. *Tectonophysics*, 488(1–4), 22–30. <https://doi.org/10.1016/j.tecto.2009.05.027>
- Reinoza, C., Jouanne, F., Audemard, F. A., Schmitz, M., & Beck, C. (2015). Geodetic exploration of strain along the El Pilar Fault in northeastern Venezuela. *Journal of Geophysical Research: Solid Earth*, 120, 1993–2013. <https://doi.org/10.1002/2014JB011483>
- Ritz, J.-F., Avagyan, A., Mkrtchyan, M., Nazari, H., Blard, P.-H., Karakhanian, A., et al. (2016). Others active tectonics within the NW and SE extensions of the Pambak-Sevan-Syunik fault: Implications for the present geodynamics of Armenia. *Quaternary International*, 395, 61–78.
- Rodriguez, M., DeMets, C., Rogers, R., Tenorio, C., Hernandez, D. (2009). A GPS and modelling study of deformation in northern Central America. *Geophysical Journal International*, 178(3), 1733–1754. <https://doi.org/10.1111/j.1365-246X.2009.04251.x>
- Rousset, B., Lasserre, C., Cubas, N., Graham, S., Radiguet, M., DeMets, C., et al. (2016). Others Lateral variations of interplate coupling along the Mexican subduction interface: Relationships with long-term morphology and fault zone mechanical properties. *Pure and Applied Geophysics*, 173(10–11), 3467–3486.
- Sagiya, T., Miyazaki, S., & Tada, T. (2000). Continuous GPS array and present-day crustal deformation of Japan. In P. Mora, M. Matsu'ura, R. Madariaga, & J. B. Minster (Eds.), *Microscopic and macroscopic simulation: Towards predictive modelling of the earthquake process* (pp. 2303–2322). Basel: Birkhäuser.
- Saria, E., Calais, E., Stamps, D. S., Delvaux, D., & Hartnady, C. J. H. (2014). Present-day kinematics of the East African Rift. *Journal of Geophysical Research: Solid Earth*, 119, 3584–3600. <https://doi.org/10.1002/2013JB010901>
- Savage, J. C., & Burford, R. O. (1973). Geodetic determination of relative plate motion in central California. *Journal of Geophysical Research*, 78(5), 832–845. <https://doi.org/10.1029/JB078i005p00832>
- Segall, P. (2002). Integrating geologic and geodetic estimates of slip rate on the San Andreas fault system. *International Geology Review*, 44(1), 62–82. <https://doi.org/10.2747/0020-6814.44.1.62>
- Shyu, J. B. H., Sieh, K., Chen, Y.-G., & Liu, C.-S. (2005). Neotectonic architecture of Taiwan and its implications for future large earthquakes. *Journal of Geophysical Research*, 110, B08402. <https://doi.org/10.1029/2004JB003251>
- Simons, W. J. F., Socquet, A., Vigny, C., Ambrosius, B. A. C., Haji Abu, S., Promthong, C., et al. (2007). Others A decade of GPS in Southeast Asia: Resolving Sundaland motion and boundaries. *Journal of Geophysical Research*, 112, B06420. <https://doi.org/10.1029/2005JB003868>
- Socquet, A., Vigny, C., Chamot-Rooke, N., Simons, W., Rangin, C., & Ambrosius, B. (2006). India and Sunda plates motion and deformation along their boundary in Myanmar determined by GPS. *Journal of Geophysical Research*, 111, B05406. <https://doi.org/10.1029/2005JB003877>
- Sornette, D., & Pisarenko, V. (2003). Fractal plate tectonics. *Geophysical Research Letters*, 30(3), 1105. <https://doi.org/10.1029/2002GL015043>
- Staller, A., Martinez-Diaz, J. J., Benito, B., Alonso-Henar, J., Hernández, D., Hernandez-Rey, R., & Diaz, M. (2016). Present-day crustal deformation along the El Salvador Fault Zone from ZFESNet GPS network. *Tectonophysics*, 670, 66–81.
- Storchak, D. A., Di Giacomo, D., Bondár, I., Engdahl, E. R., Harris, J., Lee, W. H. K., et al. (2013). Public release of the ISC-GEM global instrumental earthquake catalogue (1900–2009). *Seismological Research Letters*, 84(5), 810–815. <https://doi.org/10.1785/0220130034>
- Styron, R., Taylor, M., & Okoronkwo, K. (2010). Database of active structures from the Indo-Asian collision. *Eos Transactions American Geophysical Union*, 91(20), 181–182.
- Suito, H., & Freymueller, J. T. (2009). A viscoelastic and afterslip postseismic deformation model for the 1964 Alaska earthquake. *Journal of Geophysical Research*, 114, B11404. <https://doi.org/10.1029/2008JB005954>
- Sun, Y., Liu, M., Dong, S., Zhang, H., & Shi, Y. (2015). Active tectonics in Taiwan: Insights from a 3-D viscous finite element model. *Earthquake Science*, 28(5–6), 353–363.
- Symithe, S., Calais, E., Chabalier, J. B. D., Robertson, R., & Higgins, M. (2015). Current block motions and strain accumulation on active faults in the Caribbean. *Journal of Geophysical Research: Solid Earth*, 120, 3748–3774. <https://doi.org/10.1002/2014JB011779>
- Taylor, M., & Yin, A. (2009). Active structures of the Himalayan-Tibetan orogen and their relationships to earthquake distribution, contemporary strain field, and Cenozoic volcanism. *Geosphere*, 5(3), 199–214.
- Travis, M. E. (2012). Inter-rifting and inter-seismic strain accumulation in a propagating ridge system: A study from South Iceland. *U.S. Geological Survey*, & Paris, G. (2000). Map and database of Quaternary faults and folds in Colombia and its offshore regions, US Geological Survey.
- Veloza, G., Styron, R., Taylor, M., & Mora, A. (2012). Open-source archive of active faults for northwest South America. *Gsa Today*, 22(10), 4–10.

- Ventura, B. M., Serpelloni, E., Argnani, A., Bonforte, A., Bürgmann, R., Anzidei, M., et al. (2014). Fast geodetic strain-rates in eastern Sicily (southern Italy): New insights into block tectonics and seismic potential in the area of the great 1693 earthquake. *Earth and Planetary Science Letters*, 404, 77–88.
- Vernant, P., Reilinger, R., & McClusky, S. (2014). Geodetic evidence for low coupling on the Hellenic subduction plate interface. *Earth and Planetary Science Letters*, 385, 122–129. <https://doi.org/10.1016/j.epsl.2013.10.018>
- Wallace, L. M., Barnes, P., Beavan, J., Van Dissen, R., Litchfield, N., Mountjoy, J., et al. (2012). The kinematics of a transition from subduction to strike-slip: An example from the central New Zealand plate boundary. *Journal of Geophysical Research*, 117, B02405. <https://doi.org/10.1029/2011JB008640>
- Wallace, L. M., & Beavan, J. (2010). Diverse slow slip behavior at the Hikurangi subduction margin, New Zealand. *Journal of Geophysical Research*, 115, B12402. <https://doi.org/10.1029/2010JB007717>
- Wallace, L. M., Beavan, J., & McCaffrey, R. (2004). Subduction zone coupling and tectonic block rotations in the North Island, New Zealand. *Journal of Geophysical Research*, 109, B12406. <https://doi.org/10.1029/2004JB003241>
- Wallace, L. M., Beavan, J., McCaffrey, R., Berryman, K., & Denys, P. (2007). Balancing the plate motion budget in the South Island, New Zealand using GPS, geological and seismological data. *Geophysical Journal International*, 168(1), 332–352.
- Wallace, L. M., Ellis, S., Little, T., Tregoning, P., Palmer, N., Rosa, R., et al. (2014). Continental breakup and UHP rock exhumation in action: GPS results from the Woodlark Rift, Papua New Guinea. *Geochemistry, Geophysics, Geosystems*, 15, 4267–4290. <https://doi.org/10.1002/2014GC005458>
- Walpersdorf, A., Manighetti, I., Mousavi, Z., Tavakoli, F., Vergnolle, M., Jadidi, A., et al. (2014). Present-day kinematics and fault slip rates in eastern Iran, derived from 11 years of GPS data. *Journal of Geophysical Research: Solid Earth*, 119, 1359–1383. <https://doi.org/10.1002/2013JB010620>
- Yu, S. B., Hsu, Y. J., Bacolcol, T., Yang, C. C., Tsai, Y. C., & Solidum, R. (2013). Present-day crustal deformation along the Philippine Fault in Luzon, Philippines. *Journal of Asian Earth Sciences*, 65, 64–74. <https://doi.org/10.1016/j.jseaes.2010.12.007>